Shock Waves (2025) 35:125–141
https://doi.org/10.1007/s00193-024-01210-4

ORIGINAL ARTICLE

Characterizing the transition between regular and Mach reflections induced by a shock wave–boundary layer interaction

S. Scharnowski[1] · R. Baidya[2] · C. J. Kähler[1]

Received: 24 April 2024 / Revised: 27 November 2024 / Accepted: 29 November 2024 / Published online: 11 January 2025

Abstract

Velocity field measurements by means of PIV are used in this work to characterize the flow in a shock wave–boundary layer interaction. For a free-stream Mach number of $M_\infty = 2.56$, the flow over a flat plate model is deflected by a 16° wedge. For these flow conditions, an unsteady dual-state solution is observed where the shock switches between a regular reflection and a Mach reflection. This non-periodic mode switching is atypical for a shock wave–boundary layer interaction and causes significant changes in the flow field. The PIV measurements enable the Mach number and the flow direction to be determined from the measured velocity. In this way, both the position of the shocks and the flow deflection across the shocks can be reliably identified. Our analysis shows that regular reflection rarely occurs and that Mach reflection with varying Mach stem height is present for about 85% of the measurement time. We provide evidence here that the transition to regular reflection is related to a temporarily thickening of the boundary layer ahead of the shock interaction, which is caused by the breathing of the separation bubble below the shock interaction. This phenomenon results in compression waves that alter the Mach number and flow direction in the region upstream of the shock system, enabling a momentary transition to a regular reflection.

Keywords High-speed flow · Compressible boundary layers · Mach reflection

1 Shock reflection

When a supersonic flow approaches a wedge, a compression shock emanating from the leading edge of the wedge is formed, over which the flow is deflected by the wedge angle. The variables of the flow change abruptly across a shock, whose location is determined by the Mach number of the flow and the deflection caused by the wedge. Pressure, temperature, and density increase abruptly and the velocity component perpendicular to the shock front is decelerated to subsonic, as discussed in Anderson [1], for example.

When an oblique shock wave interacts with a turbulent boundary layer, a complex interaction is established. Due to the sudden increase in pressure across the impinging shock and the fact that the pressure of the boundary layer edge equals the wall pressure, the flow tends to detach, resulting in a significant increase in boundary layer thickness. Downstream of the shock interaction the flow attaches again and the boundary layer recovers, as shown in Fig. 1. This results first in compression, then in expansion, and finally in compression again. The resulting shock waves and expansion waves interact with the impinging shock, as discussed in detail by Délery and Dussauge [2], for instance. The incoming shock is indicated as C_1. Due to the thickening of the boundary layer caused by the increase in pressure over C_1, the flow upstream of the impingement location of C_1 is deflected away from the wall. This results in a compression that turns into C_2, the separation shock, which abruptly deflects the incoming flow near the wall upward.

Depending on which deflections the flow experiences via the shocks C_1 and C_2, there are two ways in which these shocks may interact. For sufficiently small deflection angles (whose magnitude depends on the Mach number of the incoming flow) across C_1 and C_2, the Mach number after these shocks is large enough to allow further deflections across the shocks C_3 and C_4, such that the direction of the flow after the latter shocks is the same on both sides of the

---

Communicated by C. Goyne.

✉ S. Scharnowski
sven.scharnowski@unibw.de

[1] Institute of Fluid Mechanics and Aerodynamics,
University of the Bundeswehr Munich,
Werner-Heisenberg-Weg 39, 85577 Neubiberg, Germany

[2] Department of Mechanical Engineering, University of
Melbourne, Grattan Street, Parkville, VIC 3010, Australia

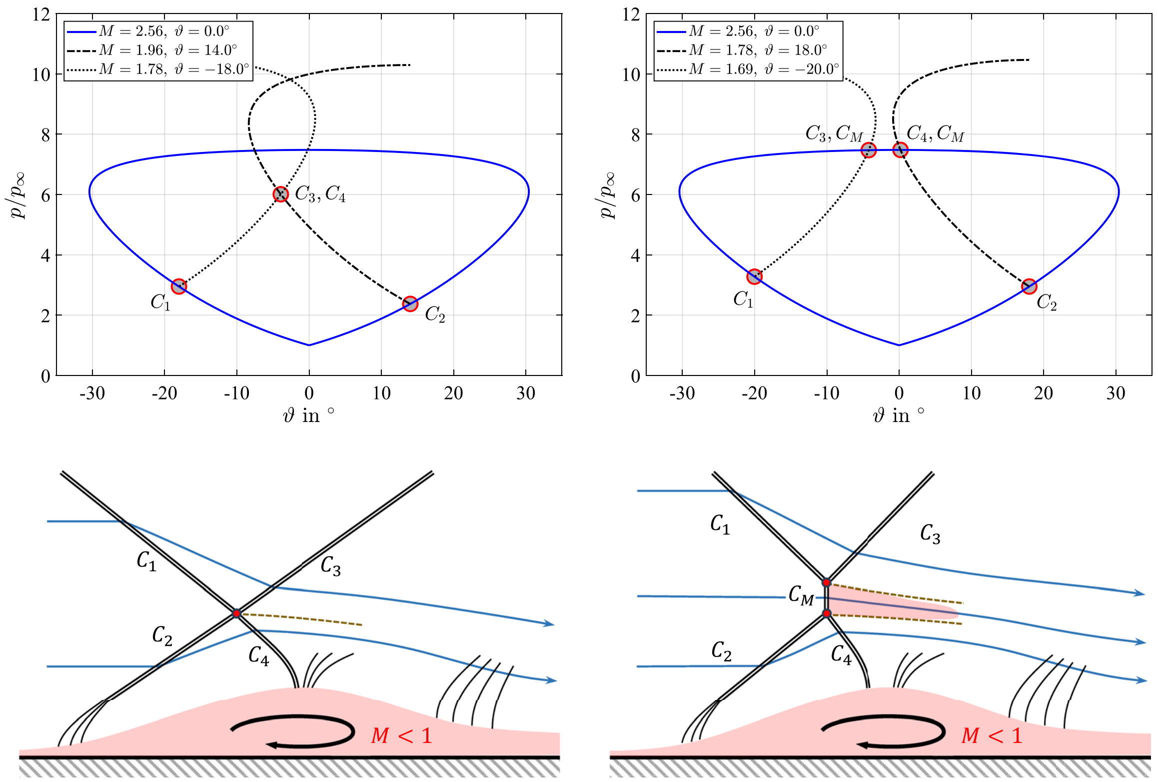

Fig. 1 Pressure–deflection diagram for a free-stream Mach number of 2.56 (top) and schematic (bottom) for the shock wave–boundary layer interaction in case of a regular reflection (left) and a Mach reflection (right)

slip line. This is a so-called regular reflection, as shown at the bottom left in Fig. 1. The top left part of the figure shows the shock polar diagram for a case with a regular reflected shock wave. The lines within the diagram represent possible solutions of pressure and flow deflection for oblique shocks from the inviscid theory for stationary two-dimensional flow. In order for the flow direction after the shocks C_3 and C_4 to be equal, it is necessary for the pressure in these two regions to be identical. In this case, there is an intersection of the dotted and the dash-dotted lines, which represent the possible shock solutions of the flow conditions downstream of C_1 and C_2. This intersection point in the shock polar diagram (labeled with C_3, C_4) determines the pressure and the flow direction for the region directly downstream of the shock interaction. However, the shape of the boundary layer thickness also determines the flow direction near the wall. Thus, the location of the shock system and the pressure downstream of the shocks are coupled to the boundary layer edge, as discussed in [2]. A contact discontinuity generally emanates from the intersection of the shocks (dashed line in the lower left part of Fig. 1), across which the pressure is the same, but the other flow variables may differ.

If the deflections across the shocks C_1 and C_2 become larger, then the lines for the shock solutions of the regions downstream of these shocks are shifted apart in the shock polar diagram. For sufficiently large deflections, there is no longer an intersection point between the dotted line and the dash-dotted line. In order to enable a continuous transition of pressure and flow direction downstream of the shock system, another shock is required. This shock is a strong solution for the incoming Mach number (solid line), which leads to a subsonic flow. The shock solutions from the regions downstream of the shocks C_1 and C_2 (dotted and dash-dotted lines) do not have a common intersection point, but they both intersect the solution of the incoming flow (solid line), as can be seen in the upper right part of Fig. 1. Instead of a point-like interaction, two triple points are established between which the shock C_M is formed, as can be seen in the bottom right of Fig. 1. Downstream of C_M, also known as Mach stem, a subsonic region can be observed that is confined by contact discontinuities (or slip lines) emanating from the two triple points. Since the upper slip line is always steeper than the lower one, the subsonic region becomes tighter and a supersonic flow forms again at some distance from the shock system. This type of reflection is called Mach reflection, which according to Ben-Dor [3] is a sub-type of irregular shock reflection.

For certain combinations of Mach number and deflection angle, both Mach reflection and regular reflection can occur. According to two-dimensional theory, the so-called dual solution domain, where both solutions can occur, exists only for Mach numbers greater than 2.202 (for perfect gas with a heat ratio of $\gamma = 1.4$) and is initially limited to a small range of flow deflection angles that increases with Mach number [4, 5]. For the transition between the two reflection types, there is generally a hysteresis for the dual solution domain [6, 7]. Whether Mach reflection or regular reflection occurs depends not only on the Mach number of the inflow and the deflection angle. Other factors that influence the occurrence of Mach reflection are the presence of side walls and the aspect ratio. Mach reflections occur at smaller wedge angles than predicted by two-dimensional theory due to the confinement of the side walls, as shown in experiments and numerical simulations [8–10]. In addition, the backpressure behind the shock wave–boundary layer interaction can cause detachment at the shock generator, thus increasing the deflection angle for C_1 and changing the reflection type, as discussed in [5, 11]. Furthermore, large-scale turbulent structures within the boundary layer locally change the flow direction and thus influence the strength of the separation shock C_2. This effect can possibly change the reflection type as shown by Matheis and Hickel [4] by means of numerical flow simulations.

In the last decades, numerous experimental investigations have been carried out on the basis of interferometry and schlieren visualizations, for example, [3, 5, 6]. This qualitative determination of the density gradients allows the topology of the shock interaction to be investigated and to check which type of reflection is present under which conditions. The reflection of a compression shock at a turbulent boundary layer has also been studied intensively in the past by means of numerical methods, see, for example, [4, 8, 12]. Since practically all flow variables are available, it is possible to investigate the influence of individual parameters in detail. In recent years, experiments on velocity field measurements using PIV have also been carried out, from which not only the location of shocks and shear layers can be determined, but also other important variables such as flow direction and velocity fluctuations [10, 13–18]. Due to the particularly good suitability of PIV for flow field analysis, this measurement technique will be used in this work to detect the shocks as well as to quantify the deflection of the flow across the shocks. This provides the opportunity to experimentally observe and understand in detail the relationship between the shock interaction and the boundary layer flow.

This work presents an experiment in which the vertical distance of the shock generator above a wall is of the same order of magnitude as the width of the test section. With an aspect ratio of 1.16 (width to distance), significant 3D effects occur which lead to irregular reflection instead of the regular reflection expected from 2D theory. The occurring shock waves interact with the turbulent boundary layer flow and show strong variations in their position which occasionally lead to a regular reflection. Thus, this study presents an experiment in which a shock is reflected in both types Mach reflection and regular reflection under the same inflow conditions. The objective of the research activity is to characterize the flow fields for both types of reflection, as well as for the transition phases, in detail. This analysis aims to explain how both types of reflection can occur under the same flow conditions and which phenomena lead to the change between the types.

After this introduction, a detailed description of the experimental setup is given in Sect. 2. This section also discusses the suitability of PIV for applications in high-speed flows. Section 3 presents the main results, including instantaneous velocity field measurements and statistical analyses. This section analyzes the differences between reflection types and how the transition between them occurs. Results are summarized, and conclusions are drawn in the last section of this work.

2 Measurement setup and methodology

Flow field measurements using particle image velocimetry (PIV) were taken in the trisonic wind tunnel Munich (TWM). For an inflow Mach number of $M_\infty = 2.56$, a shock wave was generated by means of a 16° wedge placed in the free stream above a 1.70-m-long flat plate model, which was mounted at the center of the 300-mm-wide and 675-mm-high test section. The horizontal wind tunnel walls have a slight divergence of $\pm\ 0.4°$, which compensates for the growing displacement thickness of the wall boundary layers. Two wedge-shaped supports were used to mount the shock generator outside the wall boundary layer at a distance of approximately 75 mm from the upper wall. The wedge angle of 16° is the angle between the model surface and the shock generator. For the shock generator, the leading edge was 257 mm ($\approx 19\delta_{99}$) above the top of the flat plate and its length in stream-wise direction is 155 mm ($\approx 11.5\delta_{99}$). Along the flat plate model, a well-characterized zero pressure gradient turbulent boundary layer flow develops [16, 19], onto which the compression shock impinges about 1.2 m downstream of the sharp leading edge. The stagnation pressure and the stagnation temperature of the incoming flow were $p_0 = 4.0$ bar and $T_0 = 285$ K, respectively. This leads to a free-stream velocity of $u_\infty = 570$ m/s and a Reynolds number based on the thickness of the undisturbed boundary layer at the impingement location ($\delta_{99} = 13.5$ mm) of $\mathrm{Re}_{\delta_{99}} = 5.55 \times 10^5$. Further details about the test facility are provided in [20]. The measurement parameters are summarized in Table 1.

Velocity field measurements via particle image velocimetry (PIV) were taken in the wall-normal stream-wise center plane above the model. The flow was seeded with di-

Table 1 Summary of test parameters

Property	Value
Free-stream Mach number M_∞	2.56
Free-stream velocity u_∞	570 m/s
Reynolds number $\mathrm{Re}_{\delta_{99}}$	5.55×10^5
Stagnation pressure p_0	4.0 bar
Stagnation temperature T_0	285 K
Boundary layer thickness δ_{99}	13.5 mm
Wedge angle ϑ_w	16°
Wedge tip height above plate	257 mm
Wedge length	155 mm

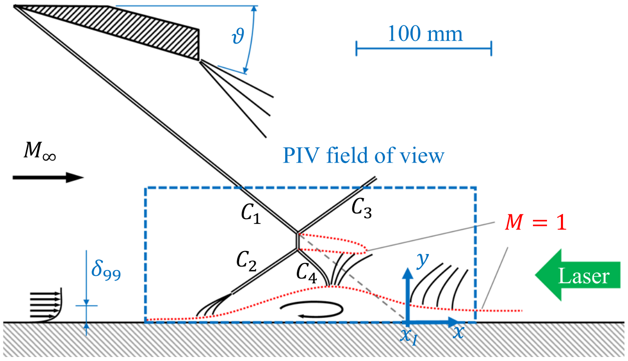

Fig. 2 Schematic representation of the experimental setup for the shock wave–boundary layer interaction experiments at the TWM. The size and position of the shock generator and the shock system as well as the boundary layer thickness are shown to scale

ethyl-hexyl sebacate (DEHS) tracer particles which have an average diameter of less than 1 µm. With a response time of approximately 2 µs [21, 22], the particles can adequately follow the flow for most of the field of view. Only for a small region around the shock is the flow velocity biased due to the following two reasons: Firstly, the inertia of the droplets in the region with strong negative acceleration causes overestimation of the fluid velocity for the first 1–2 mm downstream of the shock. Secondly, for interrogation windows through which the shock passes, the estimated velocity can have values between the velocities upstream and downstream of the shock depending on the actual shock location within the window [23]. For the relatively small magnification in these experiments, both bias errors are limited to a region of only 2–3 vectors around the shocks.

The tracers were illuminated from downstream with a wall-parallel light sheet generated by a PIV double pulse laser (DM 150-532, by Photonics Industries Inc.) with a light sheet width of about 0.5 mm. A high-speed camera (Phantom V2640, by Vision Research Inc.) equipped with a 35-mm lens (Distagon T* 35 mm f/2, by Zeiss) acquired PIV double images, 1792 × 704 pixels in size (corresponding to 245 mm×95 mm, 0.14 mm/pixel), at a recording frequency of 10 kHz. The measurement setup with the field of view is sketched in Fig. 2.

A total of 39,000 image pairs were acquired and analyzed, which corresponds to 1.6×10^5 convective time scales, based on u_∞ and δ_{99}. The number of samples is therefore considered to be well suited for statistical analyses.

The PIV measurement setup was optimized to provide an overview of the flow field to determine the position of the shocks, large-scale turbulent structures within the boundary layer, and regions with separated flow. Due to the large spatial and temporal dynamics in this type of flow, the resolution of the small-scale features is only partially possible because of the strong velocity gradients in the shear layers, as discussed in [24]. In order to enable a reliable evaluation of the PIV data, the particle image displacement was limited to 12 pixels for the free stream by setting the time separation between the image pairs to 3 µs. An iterative approach with decreasing interrogation window size and subsequent image deformation was used for the PIV image evaluation. A Gaussian window weighting function was applied and a final interrogation window size of 12^2 pixel with 50% overlap was achieved, leading to a vector grid spacing of 0.82 mm corresponding to 5.9% of δ_{99} of the undisturbed boundary layer.

In addition to the previously discussed systematic errors caused by the inertia of the particles and the window size, PIV also suffers from random errors that occur when determining the correlation maximum [25]. The magnitude of the random errors depends in particular on the number of particle images within a interrogation window and thus also on the particle image density and the window size [26, 27]. Additionally, loss-of-correlation due to velocity gradients, image noise, and light sheet mismatch affect the uncertainty [28–31]. Based on the findings in [20], the standard deviation of the displacement vectors in the undisturbed free stream is estimated to be 0.07 pixel corresponding to 0.6% of the free-stream displacement. For regions with increased turbulence or strongly three-dimensional flow, the uncertainty can be significantly larger.

Besides the velocity, the Mach number is also used for the discussion of the results in the following. For this, the local Mach number was estimated from the local velocity's absolute value U and the local speed of sound c as follows:

$$M = U/c = U/\sqrt{\gamma R T}. \tag{1}$$

Here, the local temperature T is computed using the energy equation:

$$T = T_0 - U^2 \frac{\gamma - 1}{2\gamma R}. \tag{2}$$

Here, γ is the specific heat ratio, R is the gas constant, and T_0 is the total temperature measured in the settling chamber of the wind tunnel. Based on linear error propagation, the relative error of the computed Mach number depends on the relative error of the velocity as follows:

$$\frac{\Delta M}{M} = \frac{2 \cdot \gamma R T_0}{2 \cdot \gamma R T_0 - U^2 \cdot (\gamma - 1)} \cdot \frac{\Delta U}{U}. \tag{3}$$

For small velocities, the relative errors are comparable. However, for larger velocities the relative error of the Mach number is amplified and becomes 2.3 times larger compared to the relative error of U for the free-stream velocity of 570 m/s.

3 Results and discussion

The computed velocity fields were analyzed to identify and evaluate the characteristic features of the different states and the transition between the states. In this section, a characteristic sequence of instantaneous flow fields and their temporal evolution are considered first in Sect. 3.1. Subsequently, Sects. 3.2 and 3.3 use the entire data set to provide a view on the averaged and conditional-averaged statistics to identify the flow phenomena that are specific to each type of reflection. In Sect. 3.4, space-time correlations are used to identify the relevant mechanisms that cause a transition between the different reflection types.

3.1 An instantaneous view on the transition between the reflection types

The calculated velocity fields show that the two types of reflections from Fig. 1 occur alternately and the state transition is relatively slow. In Fig. 3, a short sequence of exemplary flow fields is presented. The figure shows the flow direction on the left side and the absolute value of the wall-parallel velocity component's gradient on the right side. It is important to note that the estimated flow direction shows increased uncertainties for regions with small velocities. Furthermore, the gradient estimation suffers from bias errors in velocity estimation due to the particle lag and is therefore underestimated at the shock locations. Nevertheless, flow direction and velocity gradients are well suited for determining the shock location as well as flow defection across the shocks.

Between the successive time steps in Fig. 3, 13 additional PIV flow fields were recorded, which are not shown here. A complete video sequence is provided as supplementary material to this work. The time t at which the flow fields were acquired is normalized by the thickness of the undisturbed boundary layer without the shock interaction δ_{99} and the velocity of the free stream u_∞:

$$\tau = t \cdot u_\infty / \delta_{99}. \tag{4}$$

For the time steps in Fig. 3, thereafter τ' is used, which follows the same normalization as in (4) but is shifted such that a case of regular reflection is at $\tau' = 0$. From the PIV velocity fields, the location of the shocks was identified from the strongest gradients $\partial u/\partial x$ and $\partial v/\partial x$ and are indicated by dashed lines in the instantaneous flow fields of the figure. The x-axis and y-axis are normalized by the thickness of the undisturbed boundary layer δ_{99}, and x_I represents the extrapolated mean impingement location of the incoming shock C_1, see Fig. 2. The shock wave C_1 originating from the wedge deflects the incoming flow downward. In response to the impinging shock, the boundary layer thickness starts to increase from about $(x - x_\mathrm{I})/\delta_{99} = -10$. The suddenly growing boundary layer thickness leads to a compression of the flow, which transitions into the shock C_2, over which the flow directly above the boundary layer is deflected upward, indicated by red color in the left column of Fig. 3. The shock waves C_1 and C_2 intersect, resulting in either a regular intersection (middle row in Fig. 3) or a Mach stem with two triple points (top and bottom rows in Fig. 3).

In the right column of Fig. 3, the absolute value of the gradient of the stream-wise velocity component is shown. In addition to the shock waves which lead to a high magnitude of $\partial u/\partial x$, tangential contact discontinuities (slip lines) can also be recognized in the gradient field due to strong $\partial u/\partial y$ values. These lines separate the regions of different entropy from each other. For the cases with Mach reflection (top and bottom), two distinct slip lines emanate from the triple points of the shock interaction. During the transition to regular reflection, the Mach stem becomes smaller and the discontinuities move toward each other until they finally overlap. In the case of regular reflection, there is only one slip line, which is also much weaker since the streamlines on both sides of it have a similar upstream history.

In the case of the regular reflection in the middle row in Fig. 3, it is noticeable that the flow direction upstream of the shock system is slightly upward, i.e., the angle of the flow direction ϑ is greater than zero. The region with upward flow direction is initially limited to the section directly in front of the shock C_2 and then becomes larger until it occupies about $4\delta_{99}$ in the horizontal direction and finally collapses before Mach reflection occurs again. This change in flow direction is accompanied by a compression emanating from the boundary layer in the region between $(x - x_\mathrm{I})/\delta_{99} = -12$ and -8. The cause of this compression is probably due to the interaction of C_2 and the boundary layer, since this is where the perturbation originates. This compression weakens the shock C_2 because a reduced deflection is required, as can be seen from the gradients in Fig. 3.

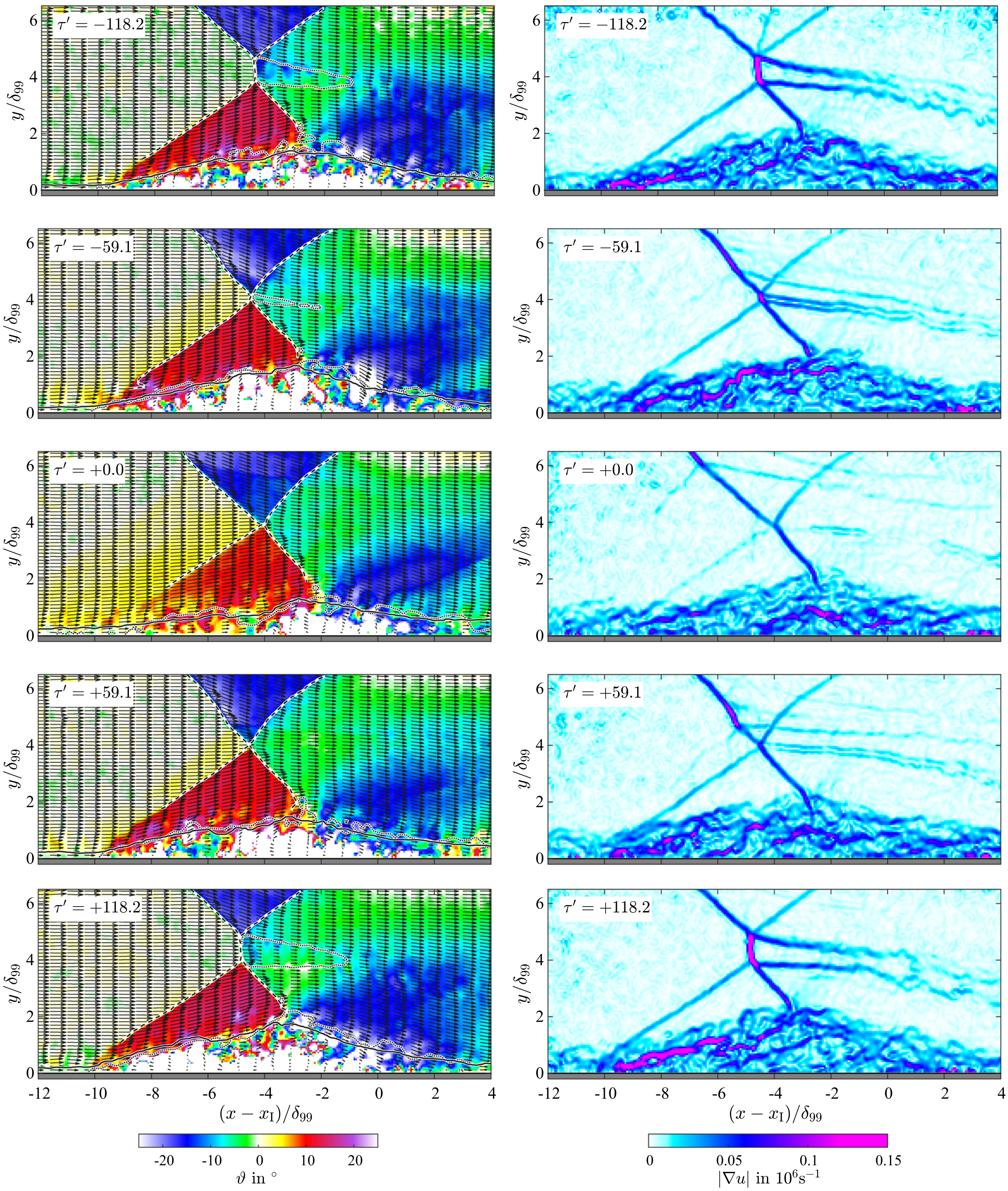

Fig. 3 On the left, instantaneous velocity fields showing the transition from Mach reflection (top) to regular reflection (middle) and back to Mach reflection (bottom). The background color represents the flow direction ϑ. The shock location, the sonic line, and the boundary layer displacement thickness are indicated by dashed, dotted, and solid lines, respectively. Velocity vectors are shown for every 10th and second grid point in x- and y-direction, respectively. On the right, the background color represents the absolute value of the wall-parallel velocity component's gradient for the same time instances as for the left side. A video sequence is provided as supplementary material to this work

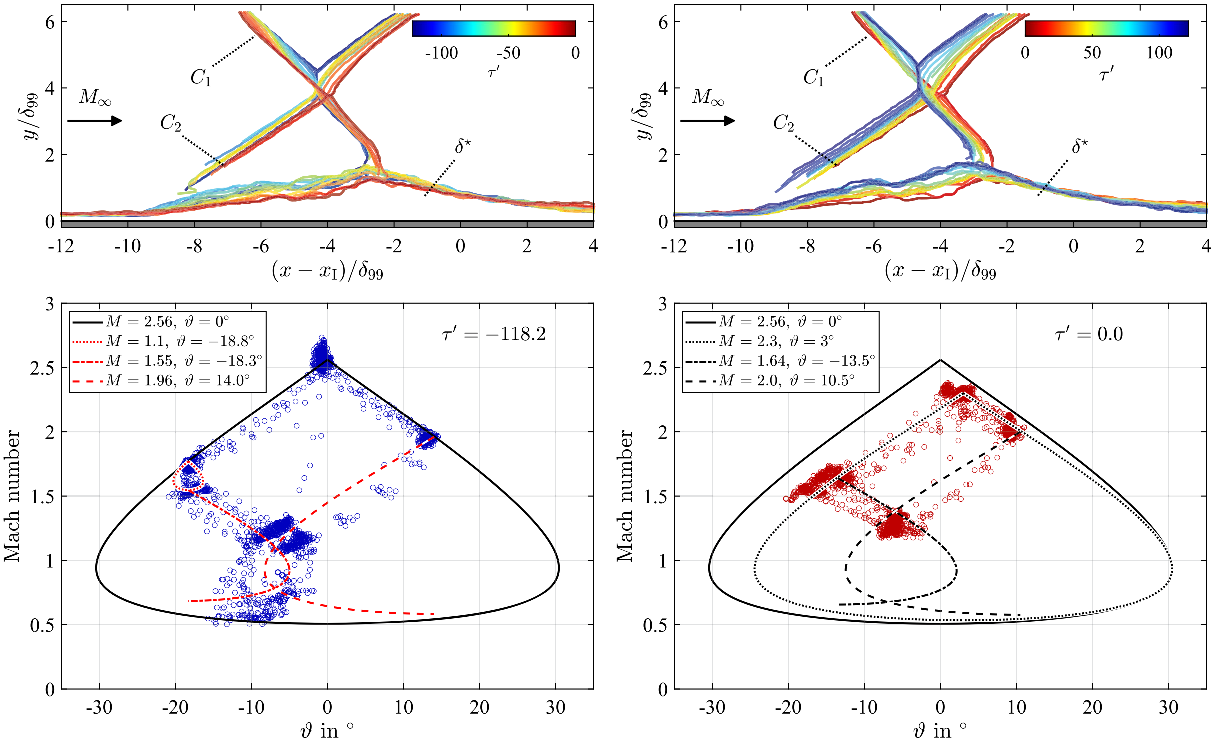

Fig. 4 Superimposed visualization of the temporal development of the shock location and displacement thickness during transition from Mach reflection to regular reflection (top left) and back to Mach reflection (top right) covering the same time span as in Fig. 3 as well as the corresponding distribution in Mach number and flow direction for Mach reflection (bottom left) and regular reflection (bottom right). The line color and symbol color indicate the elapsed time. The lines in the bottom row correspond to possible shock solutions for start conditions stated in the legends

In order to better recognize the changes in the position of the shocks and the boundary layer, Fig. 4 shows in the top row temporal evolution of the detected shock system changing from Mach reflection to regular reflection and back to Mach reflection covering the same time span as in Fig. 3. In order to see the changes in Mach number and flow direction, the bottom row of Fig. 4 shows points from the flow field around the shock system in the Mach number theta plane. The lines represent shock solutions for the incoming Mach number as well as for resulting Mach numbers.

Starting from a Mach reflection at $\tau' = -118.2$ (blue color in Fig. 4), two oblique shocks C$_1$ and C$_2$ as well as a normal shock occur for the incoming Mach number of 2.56. The values for Mach number and deflection angle in the lower left part of Fig. 4 show a clear accumulation for the shocks C$_1$ and C$_2$ at approximately $-19°$ and $+14°$, leading to Mach numbers of 1.75 and 1.96, respectively. The deflection across shock C$_1$ exceeds the wedge angle of the shock generator. This is at least partly caused by the boundary layer displacement thickness on the wedge. Additionally, the increased deflection angle may be due to the influence of the sidewalls, as previously noted by Bermejo-Moreno et al. [8] and Wang et al. [9]. The deflection over shock C$_2$ falls within the range reported in [4] for Mach numbers of 2.0 and 3.0. Downstream of the shock C$_1$, the Mach number is reduced from around 1.75–1.55 without significant changes in the flow angle. This change is not possible for a stationary shock solution; therefore, it must be an interaction with a moving wave. This reduction in the Mach number without significant changes in the flow angle can be clearly seen in Fig. 5, in which the region of shock interaction is shown enlarged. For all six time steps shown in the figure, there is an approximately normal shock between C$_1$ and C$_3$, through which the streamlines pass without being disturbed. These unexpected normal waves appear regularly during Mach reflection, as can be seen in the top part of Fig. 6 which shows the Mach number along a horizontal line at $y/\delta_{99} = 5.5$ over time.

With the reduced Mach number of approx. 1.55, the flow is redirected again across the shock C$_3$. The resulting flow direction near the upper triple point is around $-10°$ and shifts further away from the triple point to values around $-5°$. Downstream of the shock C$_2$, the flow is redirected again by the shock C$_4$, resulting in a flow direction of $-6°$ near the lower triple point, which is reduced to values around $-3°$ further away from the triple point. Between the two

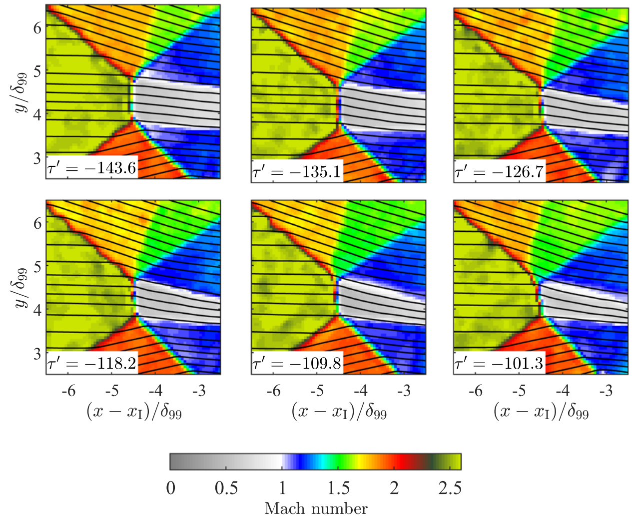

Fig. 5 Sequence of successive Mach number distributions with zoomed-in representation of the shock interaction

triple points, the flow is slowed down by a single shock, the Mach stem C_M. This is a strong shock that deflects the flow slightly toward the wall and reduces the Mach number to values around 0.52.

In the case of regular reflection at $\tau' = 0$ (red color in Fig. 4), combinations of smaller Mach numbers (around 2.3) and slightly positive angles (around $+3°$) occur in the Mach number deflection plot in the bottom right of Fig. 4. This is caused by weak compression waves emanating from the boundary layer upstream of the shock system, as visible, for example, in the middle row of Fig. 3. Note that this change in Mach number and flow direction for the region upstream of the shock system does only exist during the regular reflection. The position of the incoming shock C_1 is temporarily shifted slightly toward the wall because of the interaction with the compression waves. The shock C_2 is also shifted toward the wall, as the boundary layer below the shock is now slightly thinner. The shocks C_1 and C_2 meet approximately at the same height as the lower triple point from the Mach reflection and slightly downstream of it, as can be seen in the top row of Fig. 4. The change in flow direction across the shock C_1 is smaller for the regular reflection for the lower part of the shock and is around $-13.5°$. The deflection via C_2 is also smaller (approx. $+10°$) compared to the Mach reflection. The shocks C_3 and C_4 deflect the flow such that it has the same flow direction of about $-7°$ in the region after the interaction. This flow angle is significantly steeper than the one reported in [4] for numerical simulations at Mach numbers of 2.0 and 3.0. In the experiment shown here, the boundary layer thickness decreases faster downstream of the shock interaction. The flow direction after the shock interaction and the shock strength are coupled, and both determine the resulting flow field with the position of the shocks and the type of reflection.

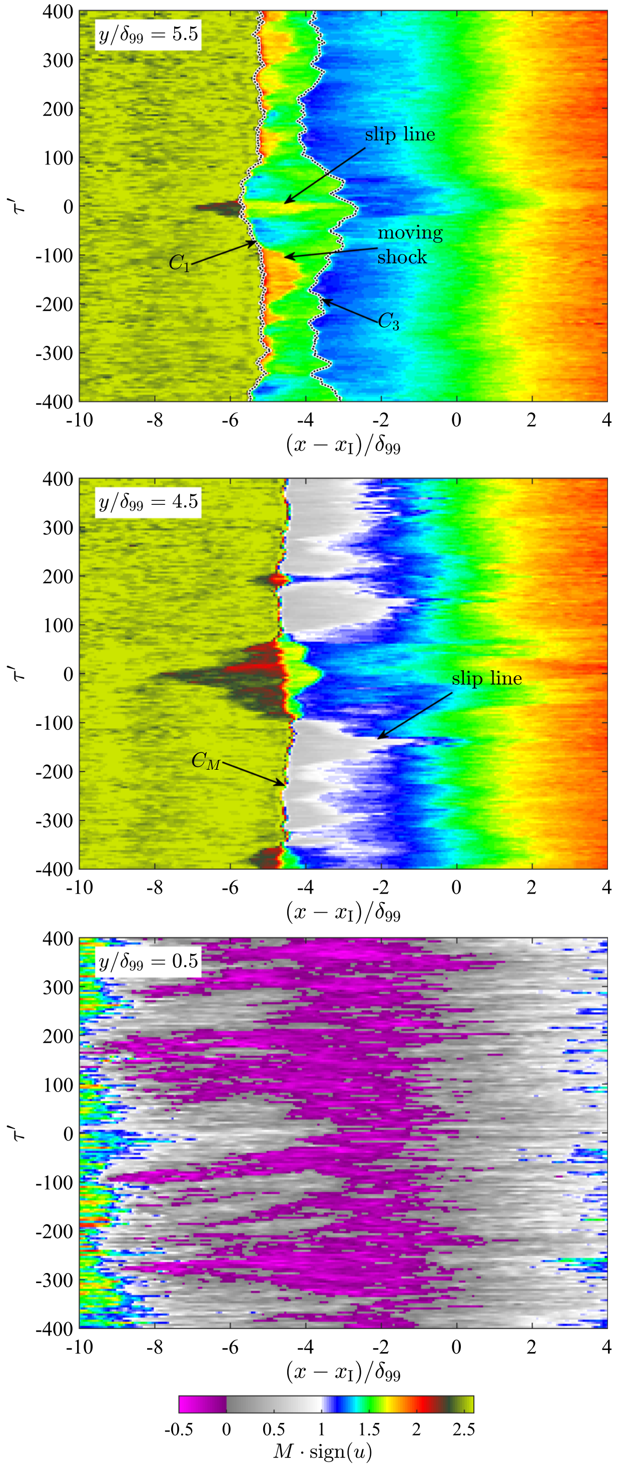

Fig. 6 Temporal development of the Mach number along horizontal lines. At the time $\tau' = 0$, the shock reflection type has changed from Mach reflection to a regular reflection

The boundary layer's displacement thickness $\delta^\star$ below the shock interaction is decreased during regular reflection. Furthermore, $\delta^\star$ is slightly thicker upstream $(x - x_\mathrm{I})/\delta_{99} < -10$ and downstream $(x - x_\mathrm{I})/\delta_{99} > 2$ of the interaction region for the red line, which corresponds to a regular reflection, as can be seen in the top row of Fig. 4. The displacement thickness therefore grows more slowly in the case of regular reflection, which also results in less deflection of the flow.

For the combination of Mach number and wedge angle investigated here, Mach reflection can be observed for most of the time, whereby the distance between the triple points and thus also the subsonic region downstream of the shock interaction varies strongly. Only rarely does the position of the triple points coincide and there is a transition to regular reflection. However, this state is obviously not stable and therefore only maintained for a few milliseconds before the Mach reflection is established again. The temporal development of the Mach number along horizontal and vertical lines is shown in Figs. 6 and 7, respectively. In Fig. 6, the data for a height of $y/\delta_{99} = 5.5$, i.e., through the shocks C_1 and C_3, for $y/\delta_{99} = 4.5$, i.e., through the shock C_M as well as close to the wall at $y/\delta_{99} = 0.5$, are shown over a time span of $\Delta\tau' = 800$. During this period, the shock C_1 moves only slightly in the plane shown and can be found between $(x - x_\mathrm{I})/\delta_{99} = -5.8$ and -5.0, as can be seen in the top of the figure. In particular, the shock C_1 shifts to smaller x-values during the regular reflection, i.e., around $\tau' = 0$, as already illustrated in Fig. 4. The compression emanating from the boundary layer interacts with the shock C_1 during the regular reflection and results in a contact discontinuity downstream of C_1, which is shown in Fig. 3 and is also visible in Fig. 6 (marked as slip line).

The shock C_3 shows much stronger variations in its x-position than C_1 and can be found between $(x - x_\mathrm{I})/\delta_{99} = -4.2$ and -2.6. In particular during regular reflection, it is strongly shifted downstream. During the Mach reflection, the previously mentioned moving shock occurs between the two shocks C_1 and C_2. As already mentioned in the discussion of Fig. 4 (bottom left), there is no static solution for such a shock. Figure 6 shows that this shock in particular is subject to strong temporal changes.

In the middle row in Fig. 6, the subsonic region downstream of the shock C_M is clearly visible. The slip line that bounds the subsonic region is characterized by strong fluctuations, as the subsonic region moves in the vertical direction and also changes its size, as already seen in Fig. 3. In the case of regular reflection, i.e., around $\tau' = 0$, the subsonic region disappears completely and the plane intersects shocks C_1 and C_3.

Near the wall at $y/\delta_{99} = 0.5$ there is subsonic flow in almost the entire field of view. Supersonic flow only exists for $(x - x_\mathrm{I})/\delta_{99} < -9$ and > 3. Flow separation occurs in this subsonic region. The size of the separated flow region varies greatly within the time range shown. The beginning of the region appears to vary considerably more than the downstream end.

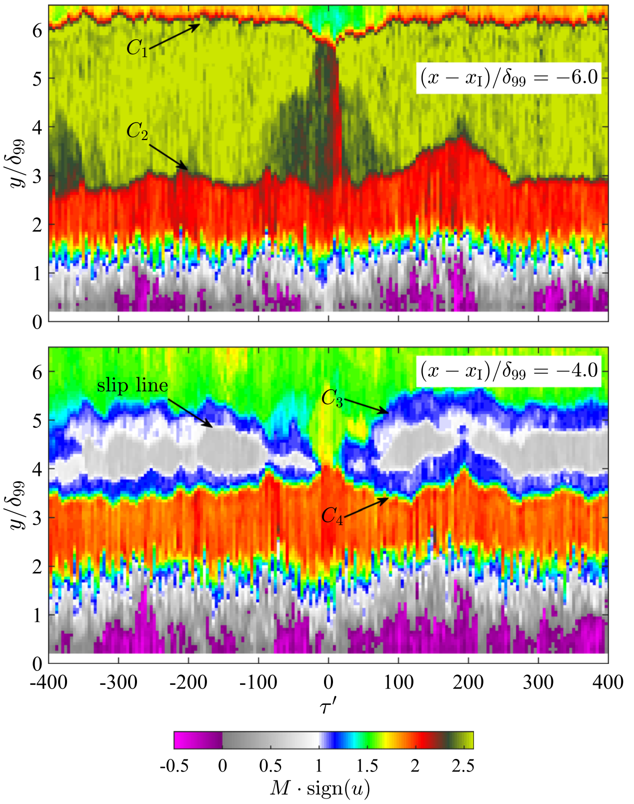

Fig. 7 Temporal development of the Mach number along vertical lines before the shock interaction at $(x - x_\mathrm{I})/\delta_{99} = -6.0$ (top) and downstream of it at $(x - x_\mathrm{I})/\delta_{99} = -4.0$ (bottom). At the time $\tau' = 0$, the shock reflection type has changed from Mach reflection to a regular reflection

Figure 7 shows the Mach number along a vertical line upstream and downstream of the shock interaction as a function of time. As seen before, the position of the shock C_1 is relatively stable, but the other shocks show strong variations in their height. In particular, C_3 moves significantly during the transition to the regular reflection, as shown in the lower part of Fig. 7. During the regular reflection, the shock C_1 is shifted downward due to the compression emanating from the boundary layer and C_2 becomes weaker and finally disappears almost completely for $\tau' = 0$, as can be seen in the upper part of Fig. 7. Downstream of the shock interaction, there are two contact discontinuities, between which there is a subsonic region. The vertical extent of the subsonic region and thus the Mach stem height and the distance between the triple points are subject to strong variations, with maximum values in the order of δ_{99} being reached. In Matheis and Hickel [4], a similar height of the Mach stem was reported for a Mach number of 2.0. However, for the case of $M_\infty = 3.0$, which has a reduced boundary layer thickness by a factor of about four, the relative Mach stem height was significantly larger. During regular reflection, both discontinuities merge and there is no subsonic zone (bottom of Fig. 7). This means that there is a significant difference in the loss of momentum downstream of the shocks for the two types of shock reflection. It is therefore important to be able to predict when there will be a change in the type of reflection.

Beneath the shock interaction, flow separation repeatedly occurs both at $(x-x_\mathrm{I})/\delta_{99}=-6.0$ and at -4.0 as can be seen from the negative flow velocity in Fig. 7. The strength of the separation does not appear to correlate directly with the type of reflection. However, it is noticeable that in the case of regular reflection, almost no backflow occurs at either position.

3.2 A statistical view on the flow field

In this section, statistical analyses of the entire dataset (39,000 velocity fields at 10 kHz, corresponding to 3.9 s or $\Delta\tau=1.65\times10^5$) are performed to determine to what extent the findings from Sect. 3.1 are generally valid and to allow a better comparison to theory and other work. Figure 8 shows the mean flow field and the velocity fluctuations. The vertical velocity component in the upper part of the figure clearly indicates the areas in which the flow was deflected. However, it is noticeable that the streamlines around the shocks do not bend sharply but are gradually deflected. This is due to the temporal variation of the shock locations. The position of the shocks is therefore not fixed but characterized by variations, as already seen in Sect. 3.1 for a short period of time. For the mean flow field, a separation region develops which extends from approx. $(x-x_\mathrm{I})/\delta_{99}=-6.8$ to -0.2 with its center at $(x-x_\mathrm{I})/\delta_{99}=-3.0$ and $y/\delta_{99}=0.4$. In the region downstream of the shock system, the streamlines directed toward the wall gradually align parallel to it. This results in a compression that appears isentropic on average but in the case of regular reflection can also contain an oblique shock (see middle line in Fig. 3).

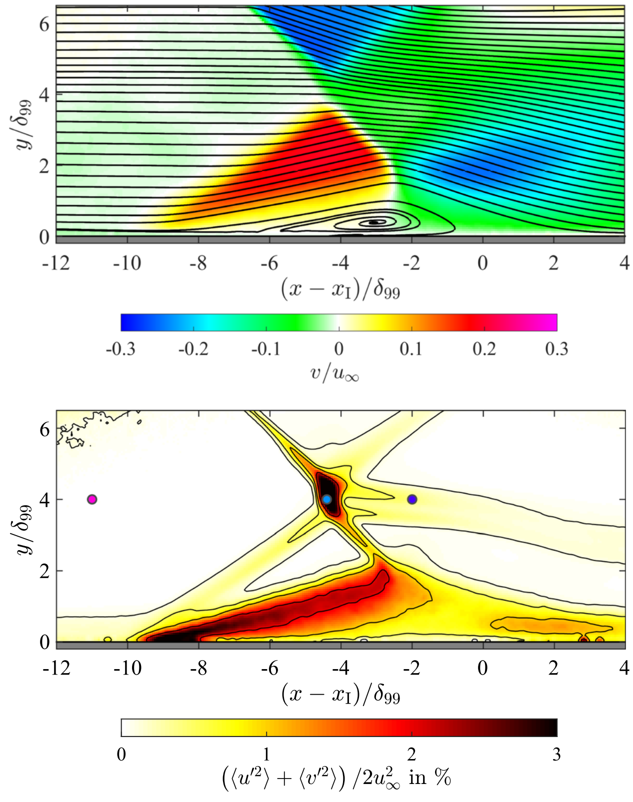

Fig. 8 Time-averaged streamlines and the distribution of the vertical velocity component v (top) as well as velocity fluctuations $\left(\langle u'^2\rangle+\langle v'^2\rangle\right)/2u_\infty^2$ with contour lines at levels of 0.1, 0.5, 1.0, and 2.0% (bottom). The markers in the lower part show the points at which the velocity over time is shown in Fig. 10

The lower part of Fig. 8 shows that increased velocity fluctuations occur mainly at the intersection of the shocks and in the detached shear layer below the shock C_2. However, significant changes in the flow velocity also occur in the area of the shocks and in a band following the streamlines downstream of the shock interaction. For the region of the shock interaction, the fluctuations are significantly larger than compared to a case with only Mach reflection in Grossman and Bruce [10]. The cause of the strong fluctuations is essentially due to the very different flow fields for the two types of reflection. The velocity fluctuations due to the shock movements, the change in shock strength, and the separated shear layer movement are superimposed on the fluctuations of the turbulence.

The separated flow region below the shock interaction exhibits significant fluctuations in size, as depicted in the bottom line of Fig. 6. Looking at the probability distribution for reversed flow in the upper part of Fig. 9, it can be seen that reversed flow occurs at least occasionally in the entire region between $(x-x_\mathrm{I})/\delta_{99}=-11$ and $+3$. At $(x-x_\mathrm{I})/\delta_{99}=-2.0$, the probability of encountering reversed flow near the wall peaks at 96.5%. In contrast to pure regular reflection at lower Mach numbers, as seen in [13, 16], where detachment only occurred for individual time steps but not on average, the separated flow occurs much more frequently. Given the higher pressure increase associated with a Mach reflection, this result was expected.

In the lower part of Fig. 9, the probability distribution of encountering subsonic flow is shown. The shape of the subsonic region near the wall reflects the development of the boundary layer. The presence of subsonic flow downstream of the shock interaction indicates Mach reflection. Since there is a local maximum of 85.6% in this region, regular reflection occurs in about 14.4% of the data. This occurrence could be less frequent if narrow subsonic regions, such as the one shown in the second line from the top in Fig. 3, are present at different heights and therefore do not all contribute to the maximum in the distribution shown in the bottom line of Fig. 9.

However, due to the spatial distribution of the backflow probability, it can be assumed that backflow and Mach reflec-

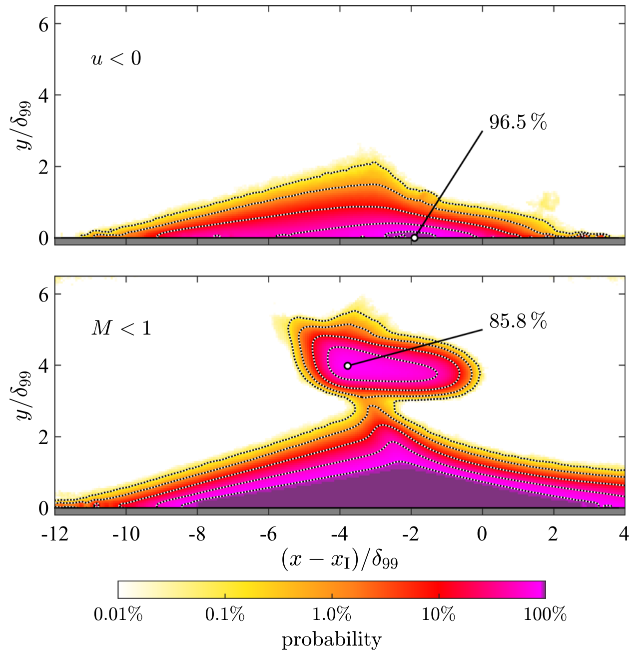

Fig. 9 Spatial distribution of the reverse flow probability (top) and the subsonic flow probability (bottom) with contour lines at levels of 0.1, 1.0, 10, 50, and 90%

tion are well correlated. Therefore, the Mach reflection can be expected to be present in about 85% of the test cases.

In order to determine whether the change between the two types of shock reflection follows a certain pattern or even whether a characteristic frequency is established, the temporal development of the velocity was analyzed at various points. Figure 10 shows in the upper part the Mach number at three points (upstream of the shock interaction, at the point with the highest fluctuations, and downstream of the interaction) for a time interval that also includes the part analyzed in Sect. 3.1 and has the same reference time. The Mach number was calculated from the velocity using (1) and (2). The fluctuations at the point before the shock interaction result mainly from the random error in the velocity measurement, which is amplified by the error propagation in estimating the temperature and Mach number. For the points at $(x - x_\mathrm{I})/\delta_{99} = -4.4$ and -2.0, it can be seen that shocks or contact discontinuities occasionally move through these points, causing the Mach number to change significantly. The lower part of the figure shows the power spectral density of the temporal development of the horizontal velocity component (full data set was used), where the PSD was calculated using Welch's method [32] with a window length of 1000 time steps (equivalent to $t = 100$ ms or $\tau \approx 4200$), an overlap of 50%, and a Hanning window function. It can be seen that neither the temporal development shows a repeated pattern nor the spectrum a dominant frequency. The transition between the two types of shock reflection therefore appears to occur non-periodically.

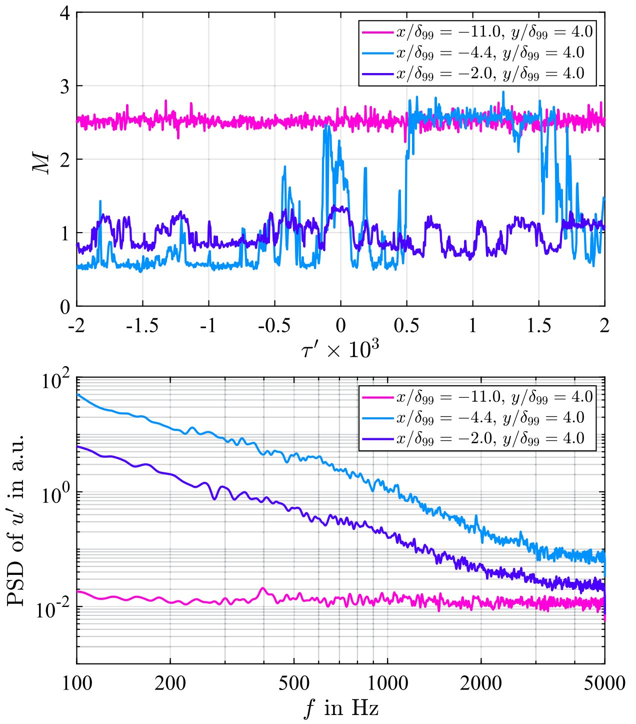

Fig. 10 Temporal development of the Mach number for a sequence of 1000 time steps (top) and power spectral density of the horizontal velocity component (bottom) for three characteristic locations, as marked in Fig. 8

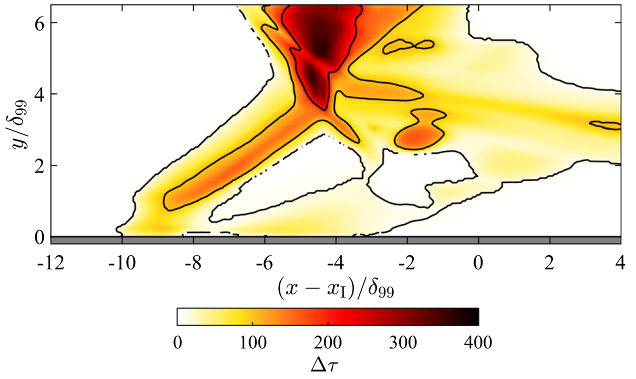

Fig. 11 Spatial distribution of the width of the auto-correlation function of the horizontal velocity component at half the height of the correlation maximum. Contour lines are shown for $\Delta\tau = 10$, 100, and 200

The auto-correlation of the velocity signal is used to determine which characteristic time scales are present in both reflection types. Figure 11 shows the width of the peak (at half height) of the auto-correlation function of the horizontal velocity component for each measurement point in the field of view. For the region upstream of the shock system, at some distance downstream of it as well as downstream of the shocks C_2 and C_4, the correlation length is so short that successive velocity fields with a temporal separation of $\Delta\tau = 4.2$ do not correlate with each other. In contrast to this, a correlation time of the order of $\Delta\tau = 100$ is achieved in the area of the shocks and even higher values of up to $\Delta\tau = 370$ are reached for the shock interaction region and between the shocks C_1 and C_3.

With a correlation time in the order of $\tau = 100$, the transition between the reflection types is a relatively slow process. Comparable frequencies corresponding to this time scale have also been found for the expansion-contraction cycle of separation bubbles in shock-wave boundary layer interactions for a compression–expansion ramp configuration [33] as well as in a shock reflection configuration [34].

3.3 A conditional-averaged view

With the aim of understanding how the flow field changes during the transition between the reflection types, the data set was divided into the different phases. The current state was determined based on the velocity downstream of the shock interaction. In a small region ranging from $(x - x_\mathrm{I})/\delta_{99} = -3.2$ to -2.3 and from $y/\delta_{99} = 3.3$ to 4.2, the spatially averaged Mach number was determined for each time step. The average Mach number in this region is a measure of the current reflection type; in the following, it is referred to as M_d. For small values of M_d, there is a pronounced subsonic area which indicates a Mach reflection. For large values of M_d, on the other hand, the subsonic region is very small or there is supersonic flow throughout, which corresponds to a regular reflection.

The histogram in Fig. 12 shows the probability of occurring values for M_d. Results between $M_\mathrm{d} = 0.6$ and 1.35 occur, and the highest probability is $M_\mathrm{d} = 0.85$. While for extremely small and extremely large values of M_d it is clear that the reflection is a Mach reflection or a regular reflection, the type of reflection cannot be clearly determined for medium values of M_d. In this transitional phase, the size of the subsonic area changes, as the triple points change their distance until they finally merge into one point meaning that there is no longer a subsonic region.

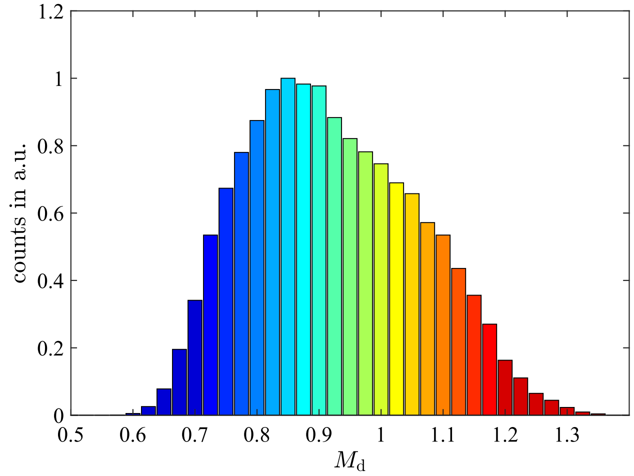

Fig. 12 Histogram of the Mach number downstream of the shock interaction M_d. Values are averaged in the region ranging from $(x - x_\mathrm{I})/\delta_{99} = -3.2$ to -2.3 and from $y/\delta_{99} = 3.3$ to 4.2

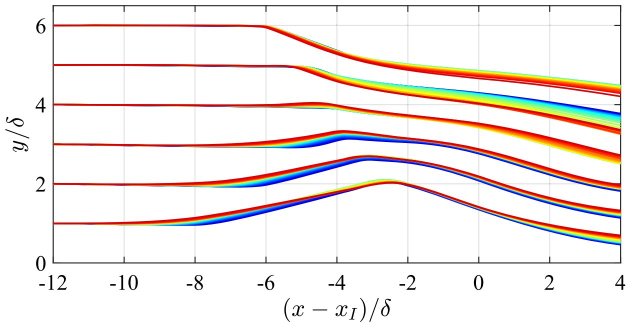

Fig. 13 Conditional-averaged streamlines starting at common upstream locations. The line color indicates the Mach number downstream of the shock interaction M_d as shown in Fig. 12

The distribution of M_d is used to conditionally average the data. Figure 13 shows streamlines of flow fields for different values of M_d. In each case, an average was taken over a width of $M_\mathrm{d} = 0.025$ and the data for values below 0.7 and above 1.2 are combined. The streamlines all start together at the left margin of the image but then diverge slightly for the different conditions.

With increasing values of M_d (change from blue to red as in Fig. 13), the streamlines running toward C_2 start to curve upward earlier and earlier. The reason for this is the aforementioned compression of the flow originating from the boundary layer (see middle line in Fig. 3). The higher the values of M_d are (i.e., the more the type of reflection approaches the regular reflection), the smaller the change in flow direction over the shock C_2. Consequently, the streamlines of the different conditions approach each other again after C_2. The compression emanating from the boundary layer also affects the shock C_1 and shifts it slightly toward the wall (see Fig. 4), which also leads to an earlier bending of the streamlines in the region of C_1. As illustrated in Fig. 13, downstream of the shock interaction, the flow occupies a larger volume in the case of Mach reflection (blue color) due to a higher momentum loss compared to regular reflection.

The conditional-averaged values for Mach number and flow direction were extracted along the streamlines from Fig. 13. The results are shown in Fig. 14 for three exemplary streamlines. At the height $y/\delta_{99} = 6.0$, the Mach number reduction in the case of regular reflection (red color) is significantly higher than in the case of Mach reflection, dropping from 2.56 to 1.4 instead of 1.75. The change in flow direction is also larger with regular reflection, as was to be expected. In the region after the shock C_1, the flow at height $y/\delta_{99} = 6.0$ is slightly slowed down in the case of regular reflection and

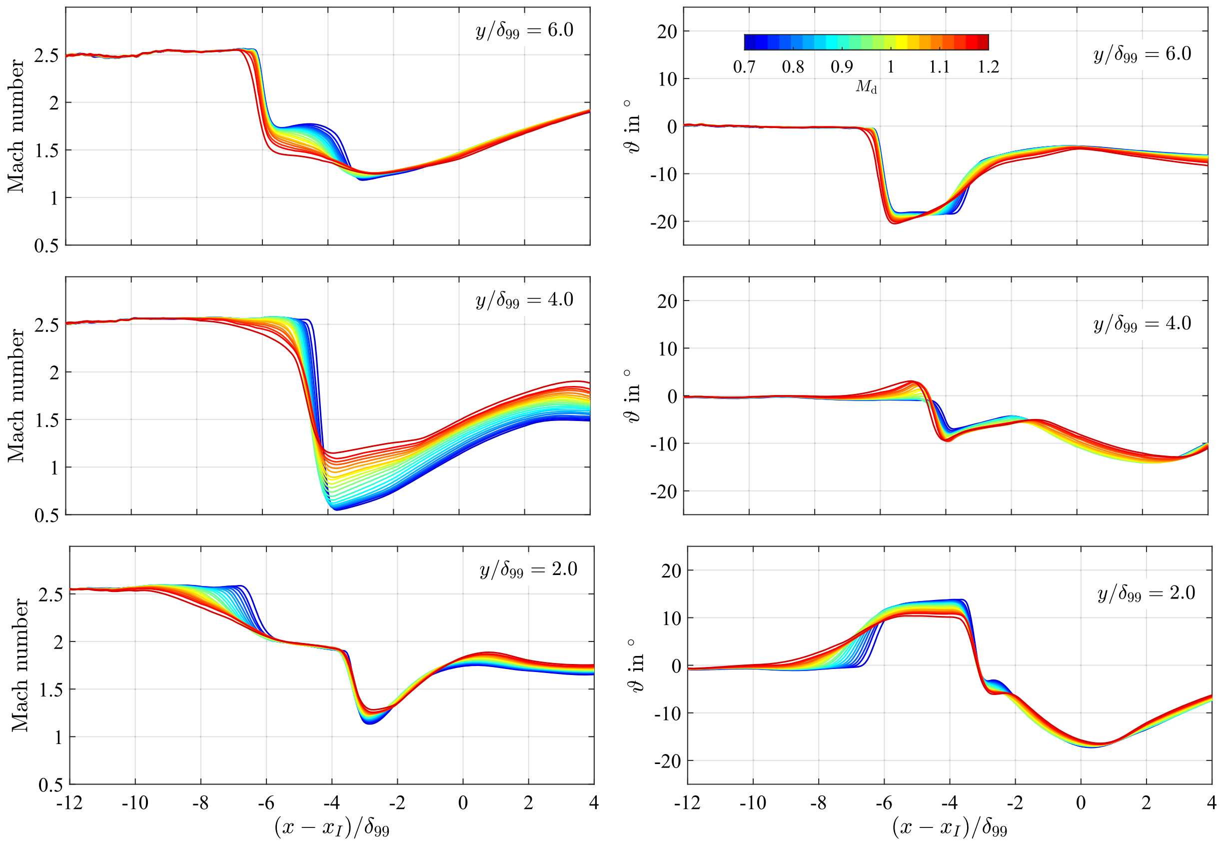

Fig. 14 Mach number (left) and flow direction (right) along the conditional-averaged streamlines starting at $y/\delta_{99} = 6.0$ (top), $y/\delta_{99} = 4.0$ (middle row), and $y/\delta_{99} = 2.0$ (bottom). The line color indicates the Mach number downstream of the shock interaction M_d as shown in Fig. 12

slightly accelerated in the case of Mach reflection. However, the flow direction changes significantly only in the case of regular reflection, as can be seen from the red line in the upper right of Fig. 13. The shock C_3 shows changes in Mach number and deflection in the case of Mach reflection (blue line), as would be expected according to theory. In the case of regular reflection, both variables appear to change only gradually. This is because the shock is relatively weak and subject to strong motion (see Fig. 4).

At the height $y/\delta_{99} = 4.0$, the streamlines are passing through the strong shock C_M in the case of Mach reflection resulting in a subsonic Mach number, as can be seen from the left part in the middle row of Fig. 14. In the case of regular reflection, the Mach number remains in the supersonic range according to theory, but there is a reduction in Mach number ahead of the shock system due to the compression described above. The flow direction is turned upward by up to 3° by the compression, but immediately after the shocks the flow is directed toward the wall in both regular reflection (up to 9.6°) and Mach reflection (about 7°). Downstream of the shock interaction, the flow is accelerated again up to $(x - x_\mathrm{I})/\delta_{99} = 3.5$, but reaches much higher Mach numbers (1.90 instead of 1.49) in the case of regular reflection.

At a height of $y/\delta_{99} = 2.0$, there is a strong influence of the compression from the boundary layer on the Mach number and the flow direction, as can be seen in the bottom line of Fig. 14. For the regular reflection (red line color), the Mach number is already reduced from $(x - x_\mathrm{I})/\delta_{99} = -11.5$ and then changes only gradually, while for the Mach reflection phase (blue) there is a rather spontaneous drop in the Mach number. After the shock C_2 up to the shock region C_4, the Mach number trends are comparable for all conditions. However, in the case of Mach reflection the conditional-averaged Mach number is reduced somewhat more over C_4 than in the case of regular reflection (to 1.13 instead of 1.28). The flow direction (bottom right in Fig. 12) shows a continuous change away from the wall for the regular reflection before shock C_2 and a rather abrupt change for the Mach reflection, as was to be expected. Between the shocks C_2 and C_4, the angle of the flow is less steep for the regular reflection and only reaches values of $\vartheta = 10°$, while it increases to $\vartheta = 13.8°$ in the case of the Mach reflection. Downstream of the shock interaction, the change in flow direction is similar for the different conditions. The Mach number on this streamline reaches a local maximum between $(x - x_\mathrm{I})/\delta_{99} = 0.4$ and 0.8 with a value between 1.75 and 1.88 for Mach reflection and regular reflection, respectively.

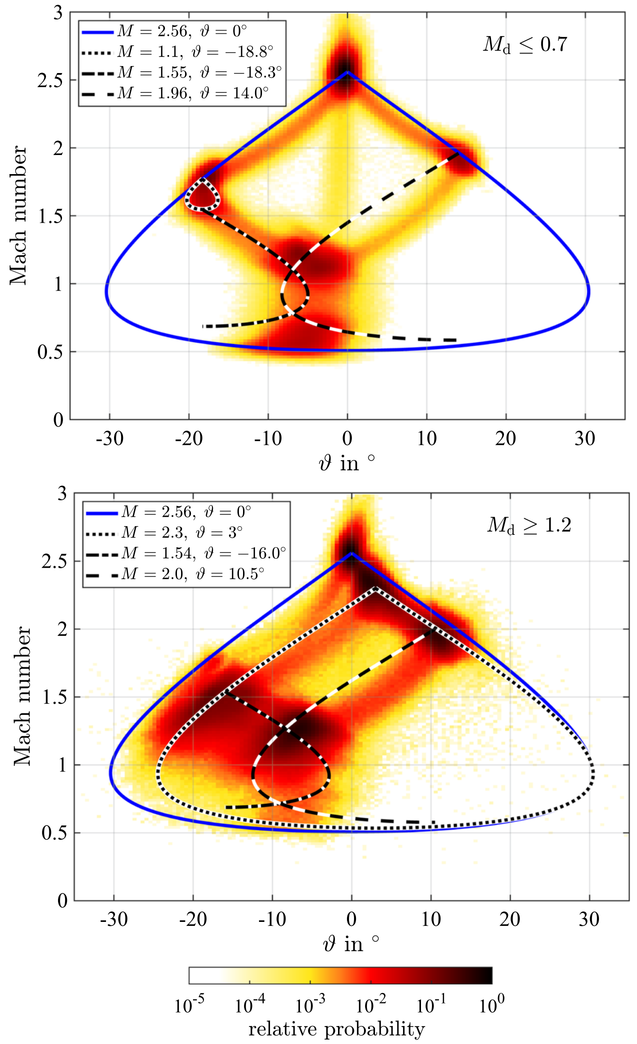

Fig. 15 Joint probability density distribution of Mach number and flow direction for the condition with the smallest Mach number downstream of the interaction (top) and highest values of M_d (bottom). The lines correspond to possible shock solutions for start conditions stated in the legends

For the two extreme cases of the Mach number downstream of the shock interaction $M_\mathrm{d} \leq 0.7$ and ≥ 1.2, Fig. 15 shows the joint probability density function for Mach number and flow direction. The lines in the figure represent possible shock solutions for occurring Mach numbers as previously shown in Fig. 4.

Although there are deviations in the values for M and ϑ within the distribution function belonging to the individual phase, the same flow phenomena are present. In the case of Mach reflection (top of Fig. 15), there is again a reduction in the Mach number between the shocks C_1 and C_3 and in the case of regular reflection (bottom), an upstream expansion influences the flow field, as discussed for Fig. 4.

Overall, it can be concluded that the flow fields from the short sequence in Sect. 3.1 are representative of the entire data set. The flow fields shown in Fig. 3 show typical events that also correspond to the extreme events of the analyzed data set.

3.4 Cause of the transition between the shock types

In the previous sections, it was shown that in the case of regular reflection the boundary layer thickens upstream of the shock C_2. The resulting compression is directly related to the transition between the reflection types. Whether the compression causes, accompanies or is a consequence of the transition between the types of shock reflection will be discussed in this section using space-time correlations of the velocity fields.

In order to identify coherent flow regions and analyze their temporal development, the two-point correlation R_{uu} of the horizontal velocity component was calculated as follows:

$$R_{uu}\left(x_0, y_0, x, y, \delta_\tau\right) = \frac{\sum_{n=1}^{N} u_n'\left(x_0, y_0, \tau\right) \cdot u_n'\left(x, y, \tau - \delta_\tau\right)}{N \cdot \sigma_u\left(x_0, y_0\right) \cdot \sigma_u\left(x, y\right)}. \tag{5}$$

where u' and σ_u are the fluctuation values about the mean and the standard deviation, respectively. The time shift δ_τ is used to analyze the temporal evolution of the correlation distribution.

For a point upstream of the shock C_2 and within the compression caused by the boundary layer, at $(x - x_\mathrm{I})/\delta_{99} = -8.0$ and $y/\delta_{99} = 2.0$, the correlation with all other points within the field of view was calculated according to (5). A time shift between $\delta_\tau = -200$ and $+200$ was applied to find the best correlation. The maximum correlation within the analyzed interval as well as the corresponding time shift is shown in Fig. 16 for the analyzed field of view. In a stripe-like region upstream of the shock C_2, which runs through the reference point and is parallel to the shock, the velocity fluctuations correlate very strongly. This area is characterized by a reduced velocity in the case of a regular reflection. Other areas of strong correlation are located between the shocks C_1 and C_3, downstream of the center of the shock interaction, and in the region above the shear layer of the detaching boundary layer between the shock C_2 and the wall. In the area between the shocks C_1 and C_3, the velocity is reduced in the case of regular reflection, as the compression emanating from the boundary layer affects this area through the shock C_1. Downstream of the shock interaction, the velocity increases in the case of regular reflection and the subsonic region of Mach reflection disappears. This results in a strongly pronounced negative correlation in a stripe following the mean streamlines (blue in the upper part of Fig. 16). The region between the shock C_2 and the wall correlates positively with

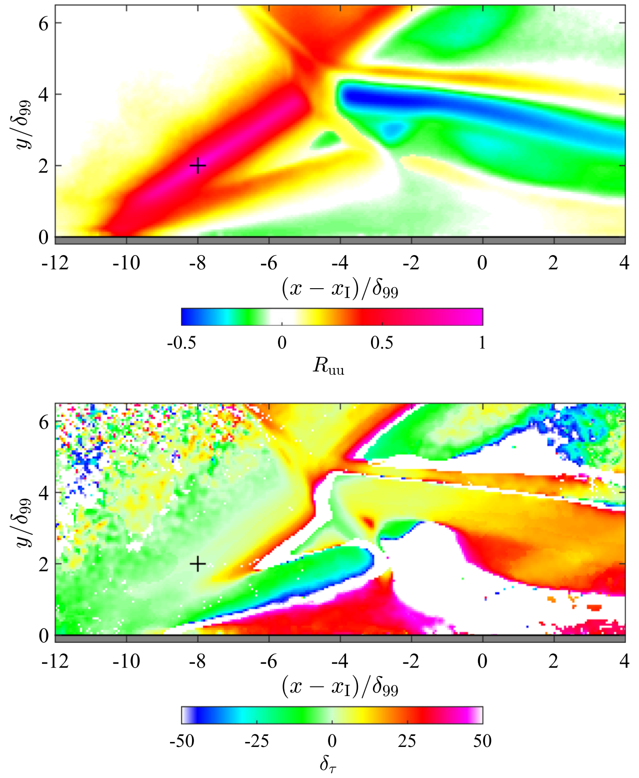

Fig. 16 Spatial distribution of the amplitude of the maximum correlation for the horizontal velocity component in the field of view compared to the reference point at $(x - x_\mathrm{I})/\delta_{99} = -8.0$ and $y/\delta_{99} = 2.0$ (top) and the corresponding time shift at which the correlation coefficient is strongest (bottom)

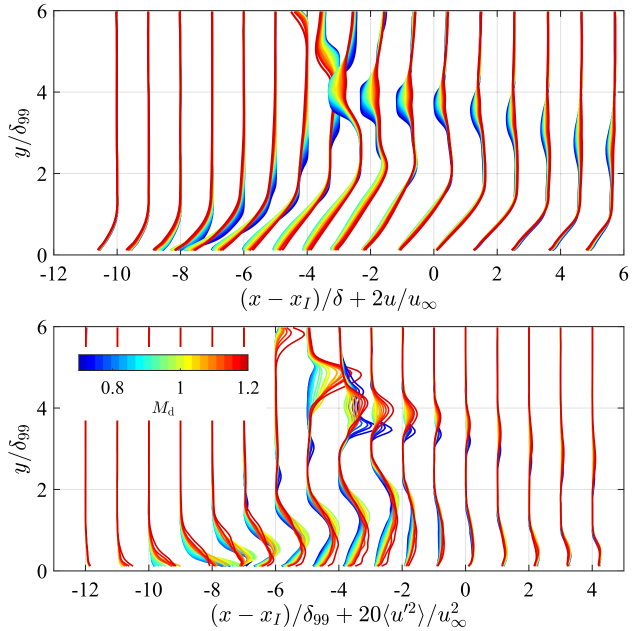

Fig. 17 Conditional-averaged profiles of the stream-wise velocity component u (top) and its fluctuations $\langle u'^2\rangle$ (bottom) for selected locations. The line color indicates the Mach number downstream of the shock interaction M_d as shown in Fig. 12

the reference point, meaning that the velocity decreases hear in the case of the regular reflection.

Regarding the time shift of the correlations, it can be seen from the bottom part of Fig. 16 that a positive time shift is required for the region upstream of C_2 and C_3 as well as for the region downstream of the center of the shock interaction. Thus, it can be concluded that the compression emanating from the boundary layer occurs first and afterward a change occurs in the region downstream of the shock interaction. Prior to the compression, however, there is a reduction in velocity in the region between the shock C_2 and the wall, as can be seen from the negative time shift in this region in the lower part of Fig. 16.

The conditional-averaged velocity profiles in Fig. 17 show that the boundary layer edge below C_2 is shifted upward in the case of regular reflection (red line color). Additionally, increased values of the fluctuations are found near the boundary layer edge (see lower part of Fig. 17), since the profiles here are less steep than in the case of Mach reflection. These increased velocity fluctuations are considered to be the cause of the thickening of the boundary layer and the resulting additional compression upstream of the shock C_2.

4 Summary and conclusions

In this work, a shock wave generated at a 16° wedge and interacting with a turbulent boundary layer flow at Mach number 2.56 has been considered with the aim to characterize the two occurring reflection types and their transition. According to the theory for two-dimensional stationary flow, the angle of the incoming shock (although increased by 3D effects) and that of the detachment shock lead to a regular reflection, as shown on the left in Fig. 1. However, in contrast to theory a Mach reflection occurs for about 85% of the observed time steps. This can be explained by the flow angle that occurs after the shock interaction. A regular reflection requires a flow angle downstream of the shock interaction which is less steep than compared to the one observed in the experiment.

Even in the case of a classical Mach reflection, as shown in Fig. 1 on the right, the measured flow angles in combination with the occurring Mach numbers (see Figs. 4, 14, and 15) are not compatible with the theory. Instead, a flow occurs in which the Mach number is further reduced in the region between shocks C_1 and C_3 without changing the direction of the flow (see Fig. 5). This is achieved by a non-stationary shock. At the same time, the flow is further decelerated by a continuous deflection after the detachment shock C_2. These phenomena are shown as a concept in the lower part of Fig. 18. In this configuration, the flow direction downstream of the shock interaction is compatible with the resulting

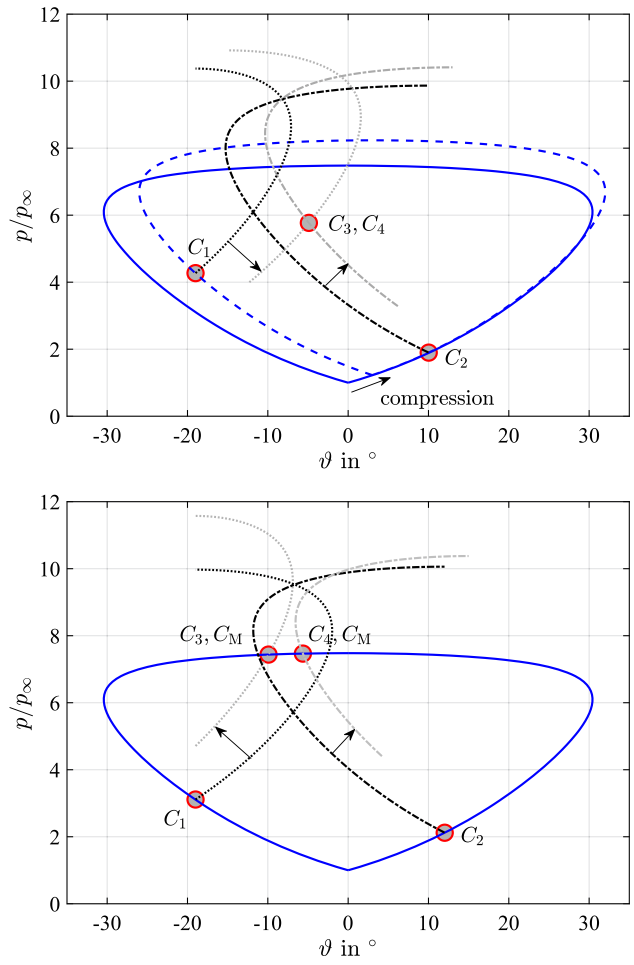

Fig. 18 Conceptual view of the phenomena occurring in the case of the investigated regular reflection (top) and Mach reflection (bottom) in the pressure–deflection plane. Gray lines indicate changes due to compression or expansion downstream of the shocks C_1 and C_2

boundary layer flow, including flow separation and reattachment.

If strong velocity fluctuations within the thickened boundary layer move away from the wall to an above-average extent, the previously described equilibrium is disturbed (see Fig. 17). The boundary layer thickens in the region where the separation shock C_2 begins, and the flow is compressed further upstream of the shock. This leads to a deflection and a reduction of the Mach number. After shocks C_1 and C_3, there is a decrease in Mach number due to further compression or unsteady waves. The resulting flow angles in the different regions, which in the end determine the pressure and the Mach number, are now compatible with a regular reflection. The concept of this configuration is shown in the upper part of Fig. 18. However, the compression in front of the shock system is not stable and the reflection type switches back to Mach reflection. On average, the duration of a regular reflection is of the order of about 100 convective time scales. The flow repeatedly switches to the Mach reflection type and remains in this state until strong fluctuations in the detached boundary layer disturb it.

Supplementary Information The online version contains supplementary material available at https://doi.org/10.1007/s00193-024-01210-4.

Acknowledgements Funding for this work was provided by the German Research Foundation (Deutsche Forschungsgemeinschaft) through research Grants (project No. 448354709), which is gratefully acknowledged.

Funding Open Access funding enabled and organized by Projekt DEAL.

References

1. Anderson, J. D.: Modern Compressible Flow With Historical Perspective, 3rd ed. McGraw Hill, New York (2003)
2. Délery, J., Dussauge, J.-P.: Some physical aspects of shock wave/boundary layer interactions. Shock Waves **19**(6), 453–468 (2009). https://doi.org/10.1007/s00193-009-0220-z
3. Ben-Dor, G.: A state-of-the-knowledge review on pseudo-steady shock-wave reflections and their transition criteria. Shock Waves **15**(3), 277–294 (2006). https://doi.org/10.1007/s00193-006-0036-z
4. Matheis, J., Hickel, S.: On the transition between regular and irregular shock patterns of shock-wave/boundary-layer interactions. J. Fluid Mech. **776**, 200–234 (2015). https://doi.org/10.1017/jfm.2015.319
5. Xue, L., Schrijer, F.F.J., van Oudheusden, B.W., Wang, C., Shi, Z., Cheng, K.: Theoretical study on regular reflection of shock wave–boundary layer interactions. J. Fluid Mech. **899**, A30 (2020). https://doi.org/10.1017/jfm.2020.455
6. Hornung, H.G., Oertel, H., Sandeman, R.J.: Transition to Mach reflexion of shock waves in steady and pseudosteady flow with and without relaxation. J. Fluid Mech. **90**(3), 541–560 (1979). https://doi.org/10.1017/S002211207900238X
7. Ben-Dor, G., Ivanov, M., Vasilev, E.I., Elperin, T.: Hysteresis processes in the regular reflection—Mach reflection transition in steady flows. Progr. Aerosp. Sci. **38**(4), 347–387 (2002). https://doi.org/10.1016/S0376-0421(02)00009-X
8. Bermejo-Moreno, I., Campo, L., Larsson, J., Bodart, J., Helmer, D., Eaton, J.K.: Confinement effects in shock wave/turbulent boundary layer interactions through wall-modelled large-eddy simulations. J. Fluid Mech. **758**, 5–62 (2014). https://doi.org/10.1017/jfm.2014.505

9. Wang, B., Sandham, N.D., Hu, Z., Liu, W.: Numerical study of oblique shock-wave/boundary-layer interaction considering sidewall effects. J. Fluid Mech. **767**, 526–561 (2015). https://doi.org/10.1017/jfm.2015.58
10. Grossman, I.J., Bruce, P.J.K.: Confinement effects on regular–irregular transition in shock-wave-boundary-layer interactions. J. Fluid Mech. **853**, 171–204 (2018). https://doi.org/10.1017/jfm.2018.537
11. Wang, C., Xue, L., Cheng, K.: Application of the minimum entropy production principle to shock reflection induced by separation. J. Fluid Mech. **857**, 784–805 (2018). https://doi.org/10.1017/jfm.2018.762
12. Ivanov, M.S., Ben-Dor, G., Elperin, T., Kudryavtsev, A.N., Khotyanovsky, D.V.: The reflection of asymmetric shock waves in steady flows: a numerical investigation. J. Fluid Mech. **469**, 71–87 (2002). https://doi.org/10.1017/S0022112002001799
13. Humble, R.A., Scarano, F., Van Oudheusden, B.W.: Unsteady aspects of an incident shock wave/turbulent boundary layer interaction. J. Fluid Mech. **635**, 47–74 (2009). https://doi.org/10.1017/S0022112009007630
14. Erdem, E., Kontis, K., Johnstone, E., Murray, N.P., Steelant, J.: Experiments on transitional shock wave-boundary layer interactions at Mach 5. Exp. Fluids **54**(10), 1598 (2013). https://doi.org/10.1007/s00348-013-1598-z
15. Giepman, R.H.M., Schrijer, F.F.J., van Oudheusden, B.W.: High-resolution PIV measurements of a transitional shock wave-boundary layer interaction. Exp. Fluids **56**(6), 113 (2015). https://doi.org/10.1007/s00348-015-1977-8
16. Baidya, R., Scharnowski, S., Bross, M., Kähler, C.J.: Interactions between a shock and turbulent features in a Mach 2 compressible boundary layer. J. Fluid Mech. **893**, A15 (2020). https://doi.org/10.1017/jfm.2020.208
17. Souverein, L.J., van Oudheusden, B.W., Scarano, F., Dupont, P.: Application of a dual-plane particle image velocimetry (dual-PIV) technique for the unsteadiness characterization of a shock wave turbulent boundary layer interaction. Meas. Sci. Technol. **20**(7), 074003 (2009). https://doi.org/10.1088/0957-0233/20/7/074003
18. Campo, L.M., Eaton, J.K.: Shock boundary layer interactions in a low aspect ratio duct. Int. J. Heat Fluid Flow **51**, 353–371 (2015). https://doi.org/10.1016/j.ijheatfluidflow.2014.10.003
19. Bross, M., Scharnowski, S., Kähler, C.J.: Large-scale coherent structures in compressible turbulent boundary layers. J. Fluid Mech. **911**, A2 (2021). https://doi.org/10.1017/jfm.2020.993
20. Scharnowski, S., Bross, M., Kähler, C.J.: Accurate turbulence level estimations using PIV/PTV. Exp. Fluids **60**(1), 1–12 (2019). https://doi.org/10.1007/s00348-018-2646-5
21. Melling, A.: Tracer particles and seeding for particle image velocimetry. Meas. Sci. Technol. **8**, 1406–1416 (1997). https://doi.org/10.1088/0957-0233/8/12/005
22. Ragni, D., Schrijer, F., Van Oudheusden, B.W., Scarano, F.: Particle tracer response across shocks measured by PIV. Exp. Fluids **50**(1), 53–64 (2011). https://doi.org/10.1007/s00348-010-0892-2
23. Kähler, C.J., Scharnowski, S., Cierpka, C.: On the resolution limit of digital particle image velocimetry. Exp. Fluids **52**, 1629–1639 (2012). https://doi.org/10.1007/s00348-012-1280-x
24. Scharnowski, S., Kähler, C.J.: Particle image velocimetry–classical operating rules from today's perspective. Opt. Lasers Eng. **135**, 106185 (2020). https://doi.org/10.1016/j.optlaseng.2020.106185
25. Sciacchitano, A.: Uncertainty quantification in particle image velocimetry. Meas. Sci. Technol. **30**(9), 092001 (2019). https://doi.org/10.1088/1361-6501/ab1db8
26. Keane, R.D., Adrian, R.J.: Theory of cross-correlation analysis of PIV images. Appl. Sci. Res. **49**, 191–215 (1992). https://doi.org/10.1007/BF00384623
27. Scharnowski, S., Sciacchitano, A., Kähler, C.J.: On the universality of Keane & Adrian's valid detection probability in PIV. Meas. Sci. Technol. **30**(3), 035203 (2019). https://doi.org/10.1088/1361-6501/aafe9d
28. Westerweel, J.: On velocity gradients in PIV interrogation. Exp. Fluids **44**, 831–842 (2008). https://doi.org/10.1007/s00348-007-0439-3
29. Scharnowski, S., Kähler, C.J.: Estimation and optimization of loss-of-pair uncertainties based on PIV correlation functions. Exp. Fluids **57**, 23 (2016). https://doi.org/10.1007/s00348-015-2108-2
30. Scharnowski, S., Kähler, C.J.: On the loss-of-correlation due to PIV image noise. Exp. Fluids **57**(7), 119 (2016). https://doi.org/10.1007/s00348-016-2203-z
31. Scharnowski, S., Grayson, K., de Silva, C.M., Hutchins, N., Marusic, I., Kähler, C.J.: Generalization of the PIV loss-of-correlation formula introduced by Keane and Adrian. Exp. Fluids **58**(10), 150 (2017). https://doi.org/10.1007/s00348-017-2431-x
32. Welch, P.D.: The use of fast Fourier transform for the estimation of power spectra: a method based on time averaging over short, modified periodograms. IEEE Trans. Audio Electroacoust. **15**, 70–73 (1967). https://doi.org/10.1109/TAU.1967.1161901
33. Grilli, M., Schmid, P.J., Hickel, S., Adams, N.A.: Analysis of unsteady behaviour in shockwave turbulent boundary layer interaction. J. Fluid Mech. **700**, 16–28 (2012). https://doi.org/10.1017/jfm.2012.37
34. Piponniau, S., Dussauge, J.-P., Debieve, J.-F., Dupont, P.: A simple model for low-frequency unsteadiness in shock-induced separation. J. Fluid Mech. **629**, 87–108 (2009). https://doi.org/10.1017/S0022112009006417